Collective states, single-particle states, and "stapler" mechanism in ^{117}In*

Hong-Fei Bai (白洪斐)[1,2] Shou-Yu Wang (王守宇)[1,2†] Xiao-Guang Wu (吴晓光)[3] Wen-Zheng Xu (许文政)[1,2]
Wen-Biao Zeng (曾文彪)[1,2] Zhi-Quan Li (李志泉)[1,2] Chen Liu (刘晨)[1,2] Hui Jia (贾慧)[4]
Bin Qi (亓斌)[1,2] En-Hong Wang (王恩宏)[1,2] Guang-Sheng Li (李广生)[3] Yun Zheng (郑云)[3]
Cong-Bo Li (李聪博)[3] Shuo Wang (王硕)[1,2] Da-Peng Sun (孙大鹏)[1,2] Xing-Chi Han (韩星池)[1,2]
Hong-Yi Zhang (张弘燚)[1,2] Nai-Bo Zhang (张乃波)[1,2]

[1]Shandong Provincial Key Laboratory of Nuclear Science, Nuclear Energy Technology and Comprehensive Utilization, Weihai Frontier Innovation Institute of Nuclear Technology, School of Nuclear Science, Energy and Power Engineering, Shandong University, Jinan 250061, China
[2]Weihai Research Institute of Industrial Technology, Shandong University, Weihai 264209, China
[3]China Institute of Atomic Energy, Beijing 102413, China
[4]School of Science, Harbin Institute of Technology, Weihai 264209, China

Abstract: High-spin states of ^{117}In are studied through the incomplete fusion reaction induced by ^{7}Li with ^{116}Cd. A total of 19 new levels and 22 new transitions are observed. A pair of signature partner bands with the $\pi(g_{7/2},d_{5/2})$ configuration is identified. The single-particle states are described through shell-model calculations. The dipole band with the configuration of $\pi g_{9/2}^{-1}\otimes\nu(h_{11/2})^2$ is proposed as a "stapler" band based on the calculations of tilted axis cranking covariant density functional theory. The "stapler" mechanism in In isotopes is systematically investigated. The present study reveals the diversity of excitation modes in ^{117}In.

Keywords: high-spin states, collective states, single-particle states, "stapler" mechanism, ^{117}In

DOI: 10.1088/1674-1137/ae38c4 **CSTR:** 32044.14.ChinesePhysicsC.50054001

I. INTRODUCTION

The underlying self-organizing mechanisms of atomic nuclei have long been a central topic at the forefront of nuclear physics. Sholars have widely recognized two primary modes of nucleonic motion in nuclei: single-particle and collective motion [1−5]. Single-particle motion typically manifests as irregular energy levels, which are commonly observed in near-spherical nuclei. Collective motion generally leads to the emergence of band structures, reflecting the underlying deformation of the nuclear shape.

It is also worth mentioning that a special excitation mode exists in near-spherical nuclei, giving rise to a strong magnetic dipole band. This band structure is believed to result from the closure of the proton and neutron angular momenta within a particle-hole configuration, referred to as the shears mechanism [6−14]. More interestingly, the competition between the shears mechanism and collective rotation of the core gives rise to a new excitation mode. In this mode, the proton (neutron) angular momentum remains nearly stationary, whereas the neutron (proton) angular momentum gradually aligns with the proton (neutron) angular momentum, significantly changing the direction of the total angular momentum. This process is analogous to the closing of a stapler, giving rise to a corresponding magnetic dipole band known as the "stapler" band [15]. Experimentally, the "stapler" band manifests as strong $M1$ transitions and weak or vanishing $E2$ transitions, which is similar to that observed in the shears mechanism. The "stapler" mechanism provides a valuable opportunity to investigate the interplay between single-particle and collective angular momentum.

To date, "stapler" bands have been suggested in ^{57}Mn [16], ^{75}As [17], ^{79}Se [18], ^{109}Ag [19], ^{115}In [15], and ^{144}Tb [20]. These nuclei are scattered across the chart of nuclides. Thus, a systematic study of the "stapler" mechanism has not been performed yet. Studying the evolution of the angular momentum components with the number of nucleons will deepen our understanding of the "stapler" mechanism and provide insight into the interplay between the shears mechanism and collective motion. In isotopes, with proton numbers close to the 50 shell closure, exhibit rich single-particle and collective structures [21−28]. Therefore, they are good candidates

Received 16 October 2025; Accepted 15 January 2026; Accepted manuscript online 16 January 2026
* Supported by the National Natural Science Foundation of China (12225504, U2167202, 12321005, 123B2081, 12475123)
† E-mail: E-mail: sywang@sdu.edu.cn

for systematically studying the evolution of the "stapler" mechanism with neutron number. In this study, the high-spin states in ^{117}In are comprehensively analyzed. The systematic variation of the "stapler" mechanisms in In isotopes is analyzed for the first time. The present study reveals the diversity of excitation modes in ^{117}In.

II. EXPERIMENTAL DETAILS

Note that ^{117}In lies on the neutron-rich side of the line of stability, which renders its high-spin states practically inaccessible via fusion-evaporation reactions using stable beam-target combinations. Recently, incomplete fusion reactions induced by ^{7}Li emerged as a promising approach for populating high-spin states of neutron-rich nuclei near the line of stability [29, 30]. As mentioned in Ref. [31], the breakup of the weakly bound ^{7}Li nucleus can produce fragments such as a proton, deuteron, triton, or helium-like nuclei (^{4}He, ^{5}He, ^{6}He). These fragments can subsequently fuse with the target. To populate high-spin states of ^{117}In, incomplete fusion reactions were performed for ^{7}Li and ^{116}Cd at 42 MeV. ^{7}Li beam was provided by the HI-13 Tandem Accelerator at the China Institute of Atomic Energy in Beijing. A self-supporting ^{116}Cd target with a thickness of 2.5 mg/cm^2 was used. The experiment was conducted for 70 h with a detection array consisting of nine HPGe detectors and two LEPS detectors. The detectors were placed at different angles with respect to the beam direction: three HPGe detectors placed at 90°, two HPGe detectors placed at 140°, two HPGe detectors placed at 42°, two HPGe detectors placed at 150°, and two LEPS detectors placed at 123°. Approximately 1.2×10^8 γ-γ coincidence events were recorded. The coincidence events were sorted into one symmetric matrix and two asymmetric matrices. The symmetric matrix was used to construct the level scheme, and the asymmetric matrices were used to extract the angular distributions from the oriented states (ADO) ratios [32] of the γ-rays. For the symmetric matrix, the x- and y-axes both correspond to events from all detectors. For the two asymmetric matrices, both the x-axes correspond to events from all detectors, whereas the y-axes correspond to events from the (i) two detectors at 42° and one detector at 150° and (ii) three detectors at 90°, respectively. The ADO ratios were determined by the ratio of the intensities I_γ(150°+42°) and I_γ(90°), *i.e.*, $R_{\rm ADO} = I_\gamma(150°+42°)/I_\gamma(90°)$. For the present geometry, the standard ADO ratios are expected to be 1.4 and 0.8 for stretched pure quadrupole and dipole transitions, respectively. In this experiment, the main reaction products included ^{119}Sb (~57%), ^{118}Sb (~20%), ^{117}In (~10%), ^{119}Sn (~4%), ^{120}Sb (~4%), ^{116}In (~3%), and ^{118}Sn (~3%). The cross section of ^{117}In calculated using PACE4 code [33, 34] only accounts for 0.46% of the total cross section, under the condition that incomplete fusion reactions are not considered. The large discrepancy between the theoretical and experimental yield ratios indicates that incomplete fusion processes play a significant role in populating high-spin states in ^{117}In. Figure 1 shows the total projection spectrum of the symmetric $\gamma-\gamma$ matrix. In this spectrum, the strong peaks from ^{119}Sb, ^{118}Sn, ^{118}Sb, and ^{117}In can be identified clearly. The origin of an obvious peak marked with a diamond is unknown. More experimental details are given in Refs. [23, 24, 26, 30, 35, 36].

III. RESULTS AND DISCUSSION

Based on the γ-γ coincidence relationships and the relative intensities of the γ-rays, a new level scheme of ^{117}In is constructed in this work , as shown in Fig. 2. The level scheme is divided into three parts and labeled as A–C for convenience of discussion. The gated spectra supporting the establishment of the present level scheme are shown in Fig. 3. The spin-parities of the known levels are adopted from the evaluated nuclear structure data file (ENSDF) [37]. For the newly observed levels, spin-parity assignments are deduced from the present measured ADO ratios. The measured γ-ray energies, relative intensities, ADO ratios, multipolarities, level energies, and spin-parity assignments of the initial and final states for the transitions in ^{117}In are summarized in Table 1.

A. Structure A

Structure A consists of bands 1 and 2, as well as four new levels on the right side of band 1, as shown in Fig. 2. The spin-parity of the 1364.9 keV level in band 2 was previously assigned as $7/2^+$ or $9/2^+$ [39]. In the present work, the ADO ratios of the 484.7 and 1364.9 keV transitions are determined as 1.32(29) and 1.27(24), respectively. These ADO ratios indicate that both transitions are either quadrupole or $\Delta I = 0$ dipole transitions. In addition, the ADO ratios of the 617.0 and 299.2 keV transitions are measured to be 0.92(25) and 0.98(22), respectively, indic-

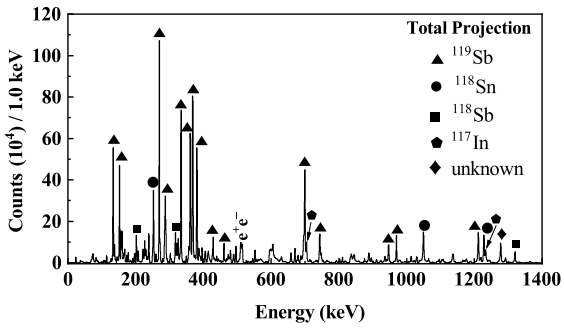

Fig. 1. Total projection spectrum of the symmetric $\gamma-\gamma$ matrix. Triangles, circles, squares, and pentagons denote transitions from ^{119}Sb, ^{118}Sn, ^{118}Sb, and ^{117}In, respectively. The diamond represents a transition of unknown origin. The transitions of ^{118}Sn are primarily from the β-decay of ^{118}Sb.

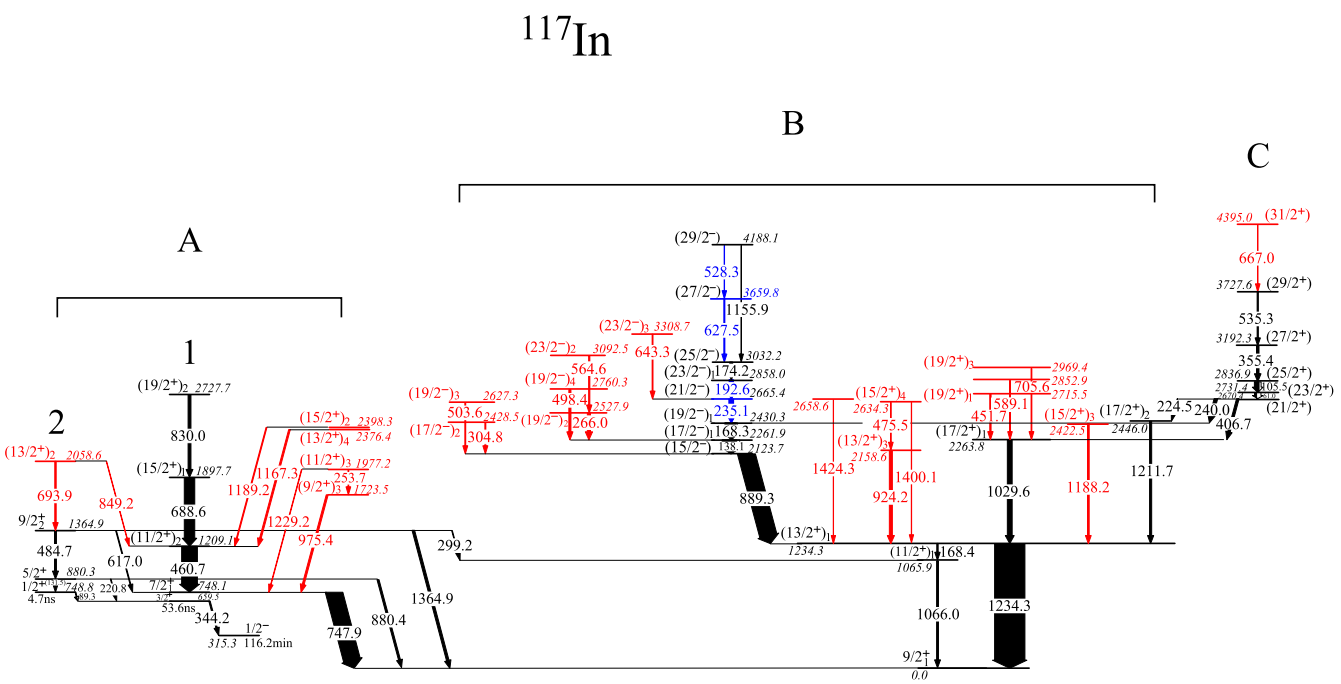

Fig. 2. (color online) Level scheme of ^{117}In deduced from the present work. The transition energies are given in keV, and the widths of the arrows are proportional to the relative transition intensities. The new transitions and levels identified in this work are marked in red. The rearranged transitions and levels are marked in blue. The 131.5 keV transition (in parentheses) is taken from Ref. [38]. The half-lives of the $1/2^-$, $3/2^+$, and $1/2^+$ levels are taken from the ENSDF [37].

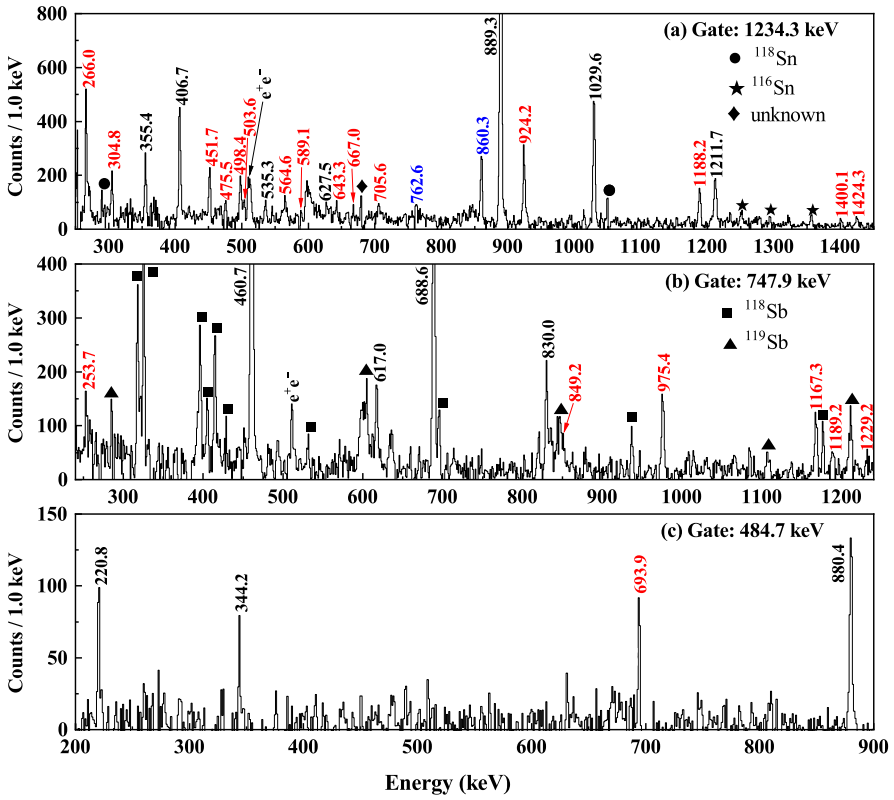

Fig. 3. (color online) γ-ray coincidence spectra gated on the (a) 1234.3 keV, (b) 747.9 keV, and (c) 484.7 keV transitions in ^{117}In. New transitions are marked in red. Transitions belonging to ^{117}In but not shown in the level scheme are in blue. Circles indicate transitions from ^{118}Sn contaminants, and stars correspond to transitions from ^{116}Sn. The diamond represents a transition of unknown origin. Squares represent contaminants from ^{118}Sb, and triangles denote those from ^{119}Sb.

Table 1. γ-ray energies, level energies of the initial and final states, relative intensities, ADO ratios, multipolarities, and spin-parity assignments of the initial and final states for the transitions in ^{117}In. The gamma-ray energy uncertainties are 0.3 keV for intense transitions ($I_\gamma \geq 10$) and 0.5 keV for weak transitions ($I_\gamma < 10$).

E_γ/keV	E_i/keV	E_f/keV	I_γ	ADO ratio	Multipolarity	$I_i^\pi \to I_f^\pi$
61.0	2731.4	2670.4	6.8(2.0)			$(23/2^+) \to (21/2^+)$
89.3	748.8	659.5	1.3(0.3)			$1/2^+ \to 3/2^+$
105.5	2836.9	2731.4	15.4(2.1)	1.13(0.22)	$M1/E2$	$(25/2^+) \to (23/2^+)$
138.1	2261.9	2123.7	47.7(3.4)	0.93(0.08)	$M1/E2$	$(17/2^-)_1 \to (15/2^-)$
168.3	2430.3	2261.9	34.0(2.5)	0.73(0.06)	$M1/E2$	$(19/2^-)_1 \to (17/2^-)_1$
168.4	1234.3	1065.9	4.0(0.9)			$(13/2^+)_1 \to (11/2^+)_1$
174.2	3032.2	2858.0	8.5(0.7)	0.84(0.11)	$M1/E2$	$(25/2^-) \to (23/2^-)_1$
192.6	2858.0	2665.4	12.8(1.0)	0.83(0.09)	$M1/E2$	$(23/2^-)_1 \to (21/2^-)$
220.8	880.3	659.5	2.6(0.3)	0.83(0.24)	$M1/E2$	$5/2^+ \to 3/2^+$
224.5	2670.4	2446.0	1.7(0.4)			$(21/2^+) \to (17/2^+)_2$
235.1	2665.4	2430.3	14.9(1.1)	0.95(0.09)	$M1/E2$	$(21/2^-) \to (19/2^-)_1$
240.0	2670.4	2430.3	11.3(0.9)	0.84(0.09)	$E1$	$(21/2^+) \to (19/2^-)_1$
253.7	1977.2	1723.5	2.3(0.5)	0.89(0.29)	$M1/E2$	$(11/2^+)_3 \to (9/2^+)_3$
266.0	2527.9	2261.9	9.2(0.8)	0.96(0.12)	$M1/E2$	$(19/2^-)_2 \to (17/2^-)_1$
299.2	1364.9	1065.9	2.1(0.6)	0.98(0.22)	$M1/E2$	$9/2_2^+ \to (11/2^+)_1$
304.8	2428.5	2123.7	3.0(0.3)	1.06(0.20)	$M1/E2$	$(17/2^-)_2 \to (15/2^-)$
344.2	659.5	315.3	4.5(0.4)	0.78(0.22)	$E1$	$3/2^+ \to 1/2^-$
355.4	3192.3	2836.9	8.1(1.4)	1.11(0.22)	$M1/E2$	$(27/2^+) \to (25/2^+)$
406.7	2670.4	2263.8	8.1(1.0)	1.50(0.17)	$E2$	$(21/2^+) \to (17/2^+)_1$
451.7	2715.5	2263.8	4.2(0.6)	0.94(0.18)	$M1/E2$	$(19/2^+)_1 \to (17/2^+)_1$
460.7	1209.1	748.1	52.0(3.9)	1.32(0.10)	$E2$	$(11/2^+)_2 \to 7/2_1^+$
475.5	2634.3	2158.6	1.9(0.3)	0.92(0.27)	$M1/E2$	$(15/2^+)_4 \to (13/2^+)_3$
484.7	1364.9	880.3	6.4(1.7)	1.32(0.29)	$E2$	$9/2_2^+ \to 5/2^+$
498.4	2760.3	2261.9	6.1(0.6)	1.05(0.17)	$M1/E2$	$(19/2^-)_4 \to (17/2^-)_1$
503.6	2627.3	2123.7	2.8(0.3)	1.40(0.29)	$E2$	$(19/2^-)_3 \to (15/2^-)$
528.3	4188.1	3659.8	1.2(0.3)			$(29/2^-) \to (27/2^-)$
535.3	3727.6	3192.3	4.0(1.0)	0.95(0.19)	$M1/E2$	$(29/2^+) \to (27/2^+)$
564.6	3092.5	2527.9	3.9(0.5)	1.26(0.27)	$E2$	$(23/2^-)_2 \to (19/2^-)_2$
589.1	2852.9	2263.8	1.6(0.3)			$\to (17/2^+)_1$
617.0	1364.9	748.1	2.6(0.4)	0.92(0.25)	$M1/E2$	$9/2_2^+ \to 7/2_1^+$
627.5	3659.8	3032.2	3.3(0.5)	1.02(0.17)	$M1/E2$	$(27/2^-) \to (25/2^-)$
643.3	3308.7	2665.4	2.8(0.4)	1.02(0.24)	$M1/E2$	$(23/2^-)_3 \to (21/2^-)$
667.0	4395.0	3727.6	1.6(0.6)			(color online) $(31/2^+) \to (29/2^+)$
688.6	1897.7	1209.1	34.8(2.6)	1.35(0.13)	$E2$	$(15/2^+)_1 \to (11/2^+)_2$
693.9	2058.6	1364.9	4.6(1.3)	1.42(0.32)	$E2$	$(13/2^+)_2 \to 9/2_2^+$
705.6	2969.4	2263.8	2.5(0.3)	0.77(0.20)	$M1/E2$	$(19/2^+)_3 \to (17/2^+)_1$
747.9	748.1	0.0	56.6(4.1)	0.95(0.08)	$M1/E2$	$7/2_1^+ \to 9/2_1^+$
830.0	2727.7	1897.7	9.5(0.9)	1.26(0.26)	$E2$	$(19/2^+)_2 \to (15/2^+)_1$
849.2	2058.6	1209.1	1.4(0.4)			$(13/2^+)_2 \to (11/2^+)_2$

Continued on next page

Table 1-continued from previous page

E_γ/keV	E_i/keV	E_f/keV	I_γ	ADO ratio	Multipolarity	$I_i^\pi \to I_f^\pi$
880.4	880.3	0.0	6.5(0.5)	1.23(0.25)	$E2$	$5/2^+ \to 9/2_1^+$
889.3	2123.7	1234.3	57.6(4.1)	0.84(0.07)	$E1$	$(15/2^-) \to (13/2^+)_1$
924.2	2158.6	1234.3	10.0(0.8)	1.23(0.14)	$M1/E2(\Delta I=0)$	$(13/2^+)_3 \to (13/2^+)_1$
975.4	1723.5	748.1	6.2(0.7)	0.78(0.13)	$M1/E2$	$(9/2^+)_3 \to 7/2_1^+$
1029.6	2263.8	1234.3	15.9(1.2)	1.37(0.14)	$E2$	$(17/2^+)_1 \to (13/2^+)_1$
1066.0	1065.9	0.0	6.1(0.7)	1.15(0.15)	$M1/E2$	$(11/2^+)_1 \to 9/2_1^+$
1155.9	4188.1	3032.2	1.0(0.3)			$(29/2^-) \to (25/2^-)$
1167.3	2376.4	1209.1	5.3(0.6)	0.72(0.12)	$M1/E2$	$(13/2^+)_4 \to (11/2^+)_2$
1188.2	2422.5	1234.3	5.5(0.5)	0.96(0.13)	$M1/E2$	$(15/2^+)_3 \to (13/2^+)_1$
1189.2	2398.3	1209.1	3.0(0.5)	1.42(0.36)	$E2$	$(15/2^+)_2 \to (11/2^+)_2$
1211.7	2446.0	1234.3	6.9(0.6)	1.39(0.29)	$E2$	$(17/2^+)_2 \to (13/2^+)_1$
1229.2	1977.2	748.1	1.1(0.3)			$(11/2^+)_3 \to 7/2_1^+$
1234.3	1234.3	0.0	100.0(5.0)	1.38(0.11)	$E2$	$(13/2^+)_1 \to 9/2_1^+$
1364.9	1364.9	0.0	8.4(2.2)	1.27(0.24)	$M1/E2(\Delta I=0)$	$9/2_2^+ \to 9/2_1^+$
1400.1	2634.3	1234.3	1.0(0.3)			$(15/2^+)_4 \to (13/2^+)_1$
1424.3	2658.6	1234.3	1.2(0.3)			$\to (13/2^+)_1$

ating that the two transitions are both stretched dipole transitions. Based on the above analysis, the assignment of $7/2^+$ to the 1364.9 keV level can be excluded. Therefore, the spin-parity of the 1364.9 keV level is assigned as $9/2^+$. The ADO ratio of the 693.9 keV transition is 1.42(32), indicating that it is either a quadrupole or $\Delta I=0$ dipole transition. Based on the assumption that spin increases with excitation energy [28, 40, 41], the spin-parity of the 2058.6 keV level is assigned as $(13/2^+)$. Band 1 has been interpreted as a negative signature partner branch of the $\pi(g_{7/2},d_{5/2})$ configuration [42]. Band 2 decays to band 1 through four $M1/E2$ transitions and has a different signature from band 1. Therefore, we suggest that band 2 is the signature partner band of band 1. Similar signature partners were observed in ^{111}In [27].

The ADO ratios of the 975.4 and 253.7 keV transitions are measured to be 0.78(13) and 0.89(29), respectively, indicating that both transitions are stretched dipole transitions. Thus, the spin-parities of the 1723.5 and 1977.2 keV levels are determined as $(9/2^+)$ and $(11/2^+)$, respectively. The ADO ratio of the 1167.3 keV transition is 0.72(12), indicating that it is a stretched dipole transition. The 1189.2 keV transition has an ADO value of 1.42(36), which suggests that it could be a quadrupole or $\Delta I=0$ dipole transition. Based on the assumption that spin increases with excitation energy, it is assigned as a quadrupole transition. Therefore, the spin-parities of the 2376.4 and 2398.3 keV levels are assigned as $(13/2^+)$ and $(15/2^+)$, respectively. Because these four levels do not form a clear band structure, only tentative interpretations based on the current level scheme are proposed in the present work. Figure 4 displays a comparison between the low-lying excited states in ^{116}Cd [43, 44] and the levels in structure A of ^{117}In. The energy of the $7/2_1^+$ level in ^{117}In is set as 0 for the convenience of comparison. As shown in Fig. 4, the $(9/2^+)_3$, $(11/2^+)_3$ and $(13/2^+)_4$, $(15/2^+)_2$ states in ^{117}In exhibit similar energies and decay behaviors to the 2_2^+ and 4_2^+ states in ^{116}Cd, respectively. Therefore, the $(9/2^+)_3$, $(11/2^+)_3$ and $(13/2^+)_4$, $(15/2^+)_2$ states in ^{117}In are tentatively interpreted as two sets of multiplets originating from the $\pi(g_{7/2},d_{5/2})\otimes$ (^{116}Cd, 2_2^+) and $\pi(g_{7/2},d_{5/2})\otimes$ (^{116}Cd, 4_2^+) configurations, respectively. The 2_2^+ and 4_2^+ states in ^{116}Cd have been explained as originating from collective vibration [44]. Thus, the $(9/2^+)_3$, $(11/2^+)_3$ and $(13/2^+)_4$, and $(15/2^+)_2$ levels in ^{117}In may also originate from vibrational excitations.

B. Structure B

Structure B includes a strong $E2$ transition to the ground state, an $M1/E2$ sequence based on the $(15/2^-)$ 2123.7 keV state, and several new transitions. The positions of the 192.6 and 235.1 keV transitions have been exchanged based on intensity considerations and the discovery of the 643.3 keV transition. Additionally, in Ref. [42], the 627.5 keV transition was placed above the 528.3 keV transition. Based on intensity considerations, their positions have also been exchanged in the current level scheme. The ADO ratio of the 924.2 keV transition is 1.23(14), and, considering a structural analogy with ^{115}In [15], it is assigned as a $\Delta I=0$ dipole transition. Therefore, the spin-parity of the newly observed 2158.6 keV level is assigned as $(13/2^+)$. For the other new levels in

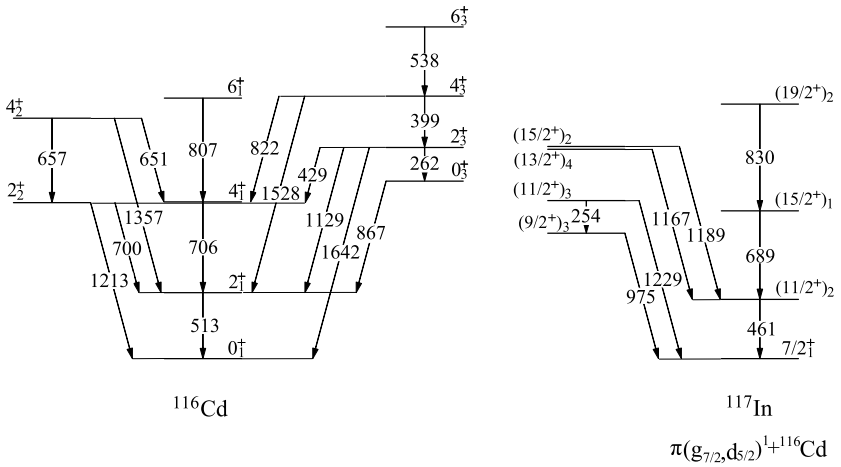

Fig. 4. Comparison of the low-lying states in ^{116}Cd [43, 44] and the levels in Structure A of ^{117}In. The energy of the $7/2_1^+$ level of ^{117}In is set as 0 for the convenience of comparison.

structure B, the spin-parity assignments are inferred from the ADO ratios of the associated transitions, under the assumption that spin increases with excitation energy.

The absence of a regular band-like structure indicates that the states in structure B may originate from single-particle excitations. Thus, shell-model calculation provides a suitable approach to describe these states. In this work, the shell-model calculations were performed for ^{117}In using the NUSHELLX code within the SNE model space [45]. The adopted two-body matrix elements are named SNET in the code [45]. The SNE model space includes eight proton orbitals ($\pi 1f_{5/2}$, $\pi 2p_{3/2}$, $\pi 2p_{1/2}$, $\pi 1g_{9/2}$, $\pi 1g_{7/2}$, $\pi 2d_{5/2}$, $\pi 2d_{3/2}$, and $\pi 3s_{1/2}$) and nine neutron orbitals ($\nu 1f_{5/2}$, $\nu 2p_{3/2}$, $\nu 2p_{1/2}$, $\nu 1g_{9/2}$, $\nu 1g_{7/2}$, $\nu 2d_{5/2}$, $\nu 2d_{3/2}$, $\nu 3s_{1/2}$, and $\nu 1h_{11/2}$). To make the calculation feasible, the following truncation was used. The $\pi 1f_{5/2}$, $\pi 2p_{3/2}$, and $\pi 2p_{1/2}$ orbitals and $\nu 1f_{5/2}$, $\nu 2p_{3/2}$, $\nu 2p_{1/2}$, and $\nu 1g_{9/2}$ orbitals were kept fully occupied. The $\pi 1g_{9/2}$ orbital was occupied by nine protons. At least six neutrons were constrained on the $\nu 1g_{7/2}$ orbital and four neutrons were constrained on the $\nu 2d_{5/2}$ orbital. No restrictions were applied to the $\nu 2d_{3/2}$ and $\nu 3s_{1/2}$ orbitals. A maximum of two neutrons were permitted in the $\nu 1h_{11/2}$ orbital.

A comparison of the calculated results with the experimental level energies is shown in Fig. 5. As shown in Fig. 5, the calculated excitation energies are in rough agreement with the experimental values. Table 2 displays the experimental and calculated level energies, as well as dominant configurations of the states in structure B. For the positive-parity states, the $9/2_1^+$ ground state is attributed to the valance proton occupying the $1g_{9/2}$ orbital. The major configuration of the $(11/2^+)_1$, $(13/2^+)_1$, and $(13/2^+)_3$ states is $\pi g_{9/2}\otimes\nu(d_{3/2}s_{1/2})^2$. The $\pi g_{9/2}\otimes\nu g_{7/2}(d_{3/2}s_{1/2})^1$ configuration formed by excitation of a neutron in the $1g_{7/2}$ orbital across the $N=64$ subshell appears at the $(13/2^+)_3$ state. This configuration dominates the $(17/2^+)_1$, $(15/2^+)_3$, and $(17/2^+)_2$ states. The $(15/2^+)_4$ and $(19/2^+)_1$ states are dominated by the $\pi g_{9/2}\otimes\nu(h_{11/2})^2$ configuration. For the negative-parity states, the lowest $(15/2^-)$ state has a three-quasiparticle configuration of $\pi g_{9/2}\otimes\nu(d_{3/2}s_{1/2})h_{11/2}$. This configuration dominates the states from $(15/2^-)$ to $(23/2^-)_1$. The neutron excitation across the $N=64$ subshell for the negative-parity states is predicted to emerge at the $(25/2^-)$ state. The three-quasiparticle $\pi g_{9/2}\otimes\nu g_{7/2}h_{11/2}$ configuration induced by the neutron cross-subshell excitation is exhausted at $27/2\hbar$. The leading configuration of the $(29/2^-)$ state is a five-quasiparticle configuration of $\pi g_{9/2}\otimes\nu g_{7/2}d_{3/2}^2h_{11/2}$, which involves both the neutron cross-subshell excitation and the breaking of a neutron pair in the $2d_{3/2}$ orbital.

Note that, although the calculated results are in rough agreement with the experimental values, the overall deviations still exist. As shown in Fig. 5, the energies of the

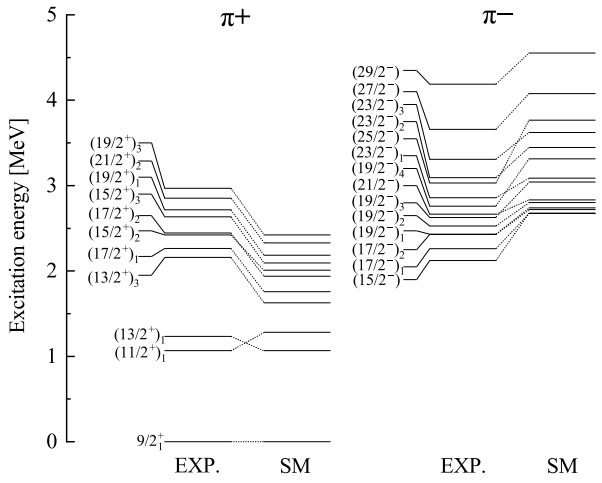

Fig. 5. Comparison of the single-particle states in structure B of ^{117}In with the results of shell-model calculations using the NUSHELLX code. The SNET interaction was used.

Table 2. Experimental and calculated level energies, as well as the dominant components of the wave functions within the SNE model space of the states in the structure B. $\pi\otimes\nu$ represents $\pi(1f_{5/2},2p_{3/2},2p_{1/2},1g_{9/2})\otimes\nu(1g_{7/2},2d_{5/2},2d_{3/2},3s_{1/2},1h_{11/2})$. The level sequence in the table is listed according to the experimental energy ordering.

J^π ($\hbar$)	$E_{\rm exp}$/MeV	$E_{\rm cal}$/MeV	Leading Configurations $\pi\otimes\nu$	Partitions (%)
$9/2_1^+$	0.0	0.0	$\pi(6,4,2,9)\otimes\nu(8,6,0,2,2)$	24.7
			$\pi(6,4,2,9)\otimes\nu(8,6,2,2,0)$	15.2
			$\pi(6,4,2,9)\otimes\nu(8,6,2,0,2)$	14.5
$(11/2^+)_1$	1.066	1.281	$\pi(6,4,2,9)\otimes\nu(8,6,1,1,2)$	41.0
$(13/2^+)_1$	1.234	1.066	$\pi(6,4,2,9)\otimes\nu(8,6,2,0,2)$	13.9
			$\pi(6,4,2,9)\otimes\nu(8,6,1,1,2)$	13.8
			$\pi(6,4,2,9)\otimes\nu(8,6,3,1,0)$	13.5
$(13/2^+)_3$	2.159	1.628	$\pi(6,4,2,9)\otimes\nu(8,6,1,1,2)$	25.0
			$\pi(6,4,2,9)\otimes\nu(7,6,2,1,2)$	14.4
$(17/2^+)_1$	2.264	1.756	$\pi(6,4,2,9)\otimes\nu(7,6,1,2,2)$	16.5
			$\pi(6,4,2,9)\otimes\nu(7,6,2,1,2)$	14.8
$(15/2^+)_3$	2.423	2.008	$\pi(6,4,2,9)\otimes\nu(7,6,2,1,2)$	20.5
			$\pi(6,4,2,9)\otimes\nu(8,6,1,1,2)$	14.9
$(17/2^+)_2$	2.446	1.939	$\pi(6,4,2,9)\otimes\nu(7,6,3,0,2)$	16.0
			$\pi(6,4,2,9)\otimes\nu(7,6,4,1,0)$	14.4
$(15/2^+)_4$	2.634	2.094	$\pi(6,4,2,9)\otimes\nu(8,6,0,2,2)$	20.7
			$\pi(6,4,2,9)\otimes\nu(7,6,2,1,2)$	17.1
$(19/2^+)_1$	2.716	2.185	$\pi(6,4,2,9)\otimes\nu(8,6,0,2,2)$	34.1
			$\pi(6,4,2,9)\otimes\nu(8,6,2,0,2)$	14.2
$(15/2^-)$	2.124	2.677	$\pi(6,4,2,9)\otimes\nu(8,6,3,0,1)$	27.0
			$\pi(6,4,2,9)\otimes\nu(8,6,2,1,1)$	24.3
			$\pi(6,4,2,9)\otimes\nu(8,6,1,2,1)$	24.3
$(17/2^-)_1$	2.262	2.674	$\pi(6,4,2,9)\otimes\nu(8,6,1,2,1)$	29.8
			$\pi(6,4,2,9)\otimes\nu(8,6,3,0,1)$	21.4
			$\pi(6,4,2,9)\otimes\nu(8,6,2,1,1)$	20.0
$(17/2^-)_2$	2.429	2.738	$\pi(6,4,2,9)\otimes\nu(8,6,1,2,1)$	57.9
$(19/2^-)_1$	2.430	2.718	$\pi(6,4,2,9)\otimes\nu(8,6,1,2,1)$	50.2
$(19/2^-)_2$	2.528	2.801	$\pi(6,4,2,9)\otimes\nu(8,6,1,2,1)$	51.8
$(19/2^-)_3$	2.627	3.041	$\pi(6,4,2,9)\otimes\nu(8,6,2,1,1)$	42.3
$(21/2^-)$	2.665	2.832	$\pi(6,4,2,9)\otimes\nu(8,6,1,2,1)$	55.7
$(19/2^-)_4$	2.760	3.314	$\pi(6,4,2,9)\otimes\nu(8,6,2,1,1)$	36.1
			$\pi(6,4,2,9)\otimes\nu(8,6,1,2,1)$	15.9
$(23/2^-)_1$	2.858	3.088	$\pi(6,4,2,9)\otimes\nu(8,6,1,2,1)$	55.8
$(25/2^-)$	3.032	3.766	$\pi(6,4,2,9)\otimes\nu(7,6,3,1,1)$	38.9
			$\pi(6,4,2,9)\otimes\nu(7,6,2,2,1)$	29.5
$(23/2^-)_2$	3.093	3.447	$\pi(6,4,2,9)\otimes\nu(8,6,2,1,1)$	45.7
			$\pi(6,4,2,9)\otimes\nu(7,6,3,1,1)$	25.2

Continued on next page

Table 2-continued from previous page

J^{π} ($\hbar$)	$E_{\rm exp}$/MeV	$E_{\rm cal}$/MeV	Leading Configurations $\pi\otimes\nu$	Partitions (%)
$(23/2^-)_3$	3.309	3.623	$\pi(6,4,2,9)\otimes\nu(7,6,3,1,1)$	29.3
			$\pi(6,4,2,9)\otimes\nu(7,6,2,2,1)$	23.1
			$\pi(6,4,2,9)\otimes\nu(7,6,4,0,1)$	22.2
$(27/2^-)$	3.660	4.078	$\pi(6,4,2,9)\otimes\nu(7,6,2,2,1)$	53.0
			$\pi(6,4,2,9)\otimes\nu(7,6,3,1,1)$	29.0
$(29/2^-)$	4.188	4.553	$\pi(6,4,2,9)\otimes\nu(7,6,2,2,1)$	47.2
			$\pi(6,4,2,9)\otimes\nu(7,6,3,1,1)$	39.4

positive-parity levels above the $(13/2^+)_1$ state are overall underestimated by approximately 0.5 MeV. By contrast, the energies of the negative-parity levels are overall overestimated by about 0.4 MeV. The observed discrepancies may not be attributed to the truncation of the active model space. The truncation employed in our calculations provides a sufficiently large active model space to describe the energy levels in structure B, for the following reasons. According to the dominant wave function components presented in Table 2, for all the states, at most one neutron in the $1g_{7/2}$ and $2d_{5/2}$ orbitals is excited across the $N = 64$ subshell. We also performed calculations that allow up to three neutrons to occupy the $1h_{11/2}$ orbital while limiting the $1g_{7/2}$ and $2d_{5/2}$ orbitals to a maximum of two neutrons for cross-subshell excitations. However, the agreement between the calculated results and experimental values did not improve; in fact, it became worse. Therefore, we attribute the discrepancies between the calculated and experimental values to the single-particle energies or the two-body matrix elements in the SNET interaction not being suitable for ^{117}In. We strongly encourage the development of effective interactions better suited for this mass region, as such efforts would enhance our understanding of the underlying mechanisms of the single-particle states. Note that in this work, only structure B was calculated using the shell-model because structures A (discussed above) and C (discussed below) likely involve collective excitations, which are not considered in the current shell-model framework.

C. Structure C

Structure C is a dipole band composed of strong $M1/E2$ transitions. It has been extended up to the $(31/2^+)$ level by adding a new transition of 667.0 keV. The dipole band has been assigned as the $\pi g_{9/2}^{-1}\otimes\nu h_{11/2}^2$ configuration [42]. Similar band structure has been observed in neighbouring ^{115}In [15]. To investigate the nature of structure C in ^{117}In, we performed the calculations of the tilted axis cranking model based on covariant density functional theory (TAC-CDFT) with the PC-PK1 parameter [46]. In the calculations, a basis of eight major harmonic oscillator shells was adopted, and pairing correlations were neglected. The calculated spins, as a function of rotational frequency, were compared with the corresponding experimental values of ^{117}In, and the results are presented in Fig. 6. Figure 6 also displays the experimental values of the band with the $\pi g_{9/2}^{-1}\otimes\nu h_{11/2}^2$ configuration of ^{115}In for comparison. As shown in Fig. 6, the experimental spin-frequency curve of structure C in ^{117}In is very similar to that of ^{115}In, and the calculations reproduce the experimental values reasonably. These agreements further support the current configuration assignment for structure C of ^{117}In.

Figure 7 shows the angular momentum vectors at rotational frequencies of 0.08 and 0.49 MeV obtained from TAC-CDFT calculations for structure C in ^{117}In. These vectors include the proton angular momentum J_π, neutron angular momentum J_ν, and total angular momentum $J_{tot} = J_\pi + J_\nu$. J_π and J_ν represent the sums of the angular momentum expectation values of all the protons and neutrons, respectively. As shown in Fig. 7, at the bandhead ($\hbar\omega \sim 0.08$ MeV), the proton and neutron angular momenta primarily align with the long and short axes, respectively. As the rotational frequency increases, the proton angular momentum J_π remains nearly stationary,

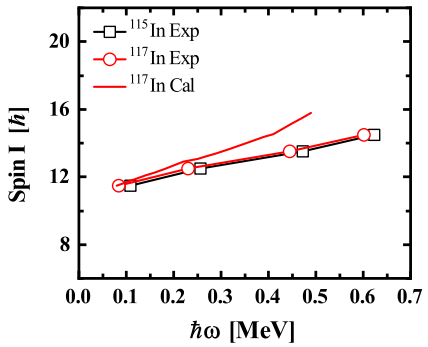

Fig. 6. (color online) Calculated spins as a function of rotational frequency obtained from the TAC-CDFT calculations in comparison with the experimental data for the structure C of ^{117}In, together with the data of the band with the $\pi g_{9/2}^{-1}\otimes\nu h_{11/2}^2$ configuration in ^{115}In. The experimental values are extracted from the relation $\hbar\omega = [E(I+1)-E(I-1)]/2$.

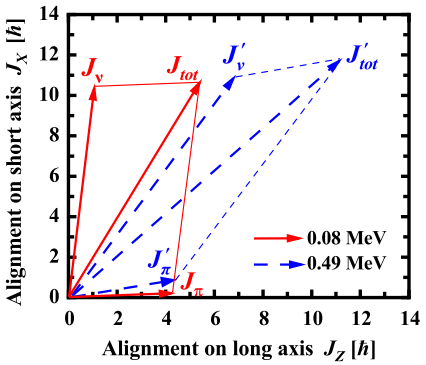

Fig. 7. Compositions of the proton, neutron, and total angular momentum vectors J_π, J_ν, and $J_{tot} = J_\pi + J_\nu$ at both rotational frequencies of 0.08 and 0.49 MeV for the $\pi g_{9/2}^{-1} \otimes \nu h_{11/2}^2$ configuration in the TAC-CDFT calculations.

whereas the neutron angular momentum J_ν gradually moves toward the direction of J_π. Consequently, the orientation of the total angular momentum exhibits a noticeable change. The evolution of the angular momenta from low to high frequencies is similar to that observed in ^{115}In, resembling the closing process of a stapler. Therefore, structure C in ^{117}In is suggested as a "stapler" band.

To further study the evolution of the "stapler" mechanism as the neutron number increases, the deformation parameters and angular momentum increment components of the "stapler" bands in ^{115}In, ^{117}In, and ^{119}In were extracted from TAC-CDFT calculations and are shown in Fig. 8. As shown in Fig. 8 (a1)-(c1), the calculated deformation parameters (β_2, γ) for the "stapler" bands of ^{115}In, ^{117}In, and ^{119}In are approximately (0.15, 52°), (0.11, 38°), and (0.09, 50°), respectively. We can observe that the deformations of the bands become smaller as the neutron number increases. The percentages of the contributions to the total angular momentum increment from the shears mechanism and core rotation at the same frequency range are displayed in Fig. 8 (a2)-(c2). Here, the angular momentum increment from the proton hole $\pi g_{9/2}^{-1}$ and two unpaired neutrons $\nu h_{11/2}^2$ is defined as the contribution of the shears mechanism and denoted as $\Delta J_{\rm shear}$. The angular momentum increment from the collective rotation of the core is defined by excluding the contributions of the shears mechanism from the total angular momentum increment and is denoted as $\Delta J_{\rm core}$. As shown in Fig. 8 (a2)-(c2), as the neutron number increases, the contribution from the shear mechanism increases, whereas that from core rotation decreases. The reduction in the proportion of $\Delta J_{\rm core}$ can be attributed to the decrease in deformation with an increase in the neutron number. To gain a deeper understanding of the "stapler" mechanism, further investigations in ^{119}In and more neutron-rich In isotopes where the collective contribution may become smaller or even vanish are highly expected.

IV. CONCLUSION

In summary, high-spin states of ^{117}In are populated through the incomplete fusion reaction of ^{7}Li with ^{116}Cd. The level scheme of ^{117}In is extended by adding 19 new

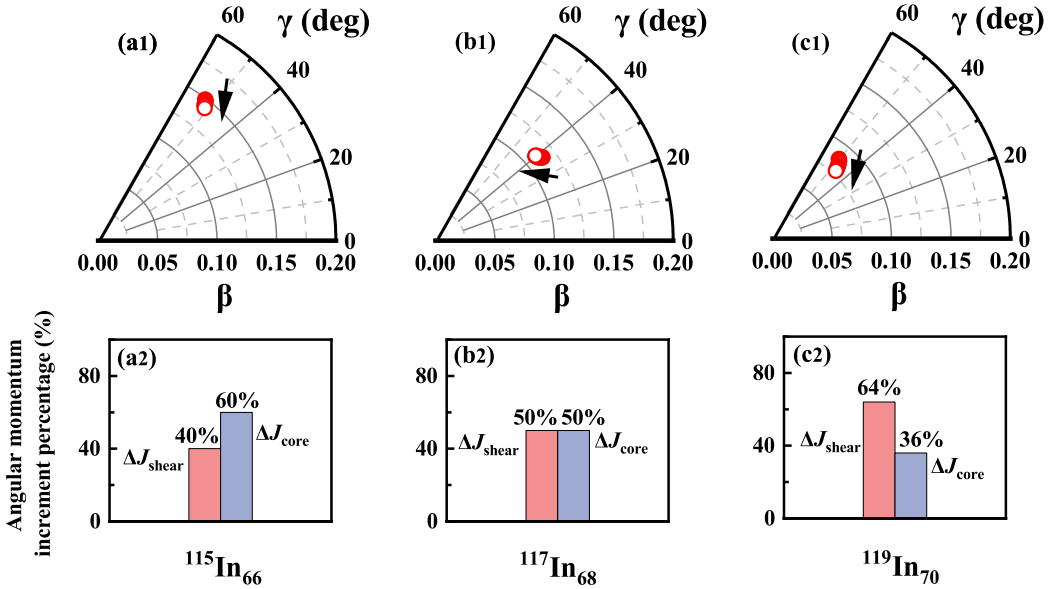

Fig. 8. (color online) Evolution of the deformation parameters β_2 and γ driven by increasing rotational frequency in the TAC-CDFT calculations for the "stapler" bands of (a1) ^{115}In, (b1) ^{117}In, and (c1) ^{119}In. The arrow indicates the increasing direction of the rotational frequency from 0.08 to 0.36 MeV. The percentages of the contributions to the total angular momentum increment for the rotational frequency of 0.08 to 0.36 MeV from the shears mechanism $\Delta J_{\rm shear}$ and core rotation $\Delta J_{\rm core}$ in the "stapler" bands of (a2) ^{115}In, (b2) ^{117}In, and (c2) ^{119}In.

levels and 22 new transitions. Bands 1 and 2 are suggested as a pair of signature partner bands based on the $\pi(g_{7/2},d_{5/2})$ configuration. The $(9/2^+)_3$, $(11/2^+)_3$ and $(13/2^+)_4$, $(15/2^+)_2$ states in structure A are tentatively interpreted as two sets of multiplets originating from the $\pi(g_{7/2},d_{5/2})\otimes(^{116}\mathrm{Cd},\,2_2^+)$ and $\pi(g_{7/2},d_{5/2})\otimes(^{116}\mathrm{Cd},\,4_2^+)$ configurations, respectively. The levels in structure A are indicative of the collective modes in ^{117}In. The states in structure B are described by shell-model calculations and represent the results of single-particle motion in ^{117}In. The dipole band with the $\pi g_{9/2}^{-1}\otimes\nu(h_{11/2})^2$ configuration is proposed as a "stapler" band based on the TAC-CDFT calculations. The systematic analysis of the angular momentum increment components shows that the contribution from core rotation becomes smaller with the increasing neutron number for $N\geqslant 66$ In isotopes. The presence of collective excitations, single-particle excitations, and the "stapler" mechanism reveals the diversity of excitation modes in ^{117}In. The "stapler" mode in ^{117}In can be further analyzed through g-factor measurements and by determining transition probabilities through lifetime measurements.

ACKNOWLEDGEMENTS

The authors would like to thank the staff of the China Institute of Atomic Energy (CIAE) for their technical support during the experiment. We also acknowledge the super-computing system at Shandong University, Weihai, for providing the computational resources necessary for the numerical calculations in this paper.

References

[1] I. Stefanescu, G. Georgiev, D. L. Balabanski *et al.*, Phys. Rev. Lett. **100**, 112502 (2008)
[2] J. Luis Egido, Marta Borrajo and Tomás R. Rodríguez, Phys. Rev. Lett. **116**, 052502 (2016)
[3] R. J. Guo, S. Y. Wang, C. Liu *et al.*, Phys. Rev. Lett. **132**, 092501 (2024)
[4] Y. Ichikawa, H. Nishibata, Y. Tsunoda *et al.*, Nat. Phys. **15**, 321 (2019)
[5] T. Otsuka, Y. Tsunoda, T. Abe *et al.*, Phys. Rev. Lett. **123**, 222502 (2019)
[6] S. Frauendorf, Nucl. Rhys. A **557**, 259 (1993)
[7] R. M. Clark and A. O. Macchiavelli, Annu. Rev. Nucl. Part. Sci. **50**, 1 (2000)
[8] S. Frauendorf, Rev. Mod. Phys. **73**, 463 (2001)
[9] H. Hübel, Prog. Par. Nucl. Phys. **54**, 1 (2005)
[10] J. Meng, J. Peng, S. Q. Zhang *et al.*, Front. Phys. **8**, 55 (2013)
[11] R. M. Clark, S. J. Asztalos, G. Baldsiefen *et al.*, Phys. Rev. Lett. **78**, 1868 (1997)
[12] H. Schnare, R. Schwengner, S. Frauendorf *et al.*, Phys. Rev. Lett. **82**, 4408 (1999)
[13] R. M. Clark, S. J. Asztalos, B. Busse *et al.*, Phys. Rev. Lett. **82**, 3220 (1999)
[14] D. G. Jenkins, R. Wadsworth, J. A. Cameron *et al.*, Phys. Rev. Lett. **83**, 500 (1999)
[15] Z. Q. Chen, S. Y. Wang, L. Liu *et al.*, Phys. Rev. C **91**, 044303 (2015)
[16] J. Peng and W. Q. Xu, Chin. Phys. Lett. **33**, 012101 (2016)
[17] C. G. Li, Q. B. Chen, S. Q. Zhang *et al.*, Phys. Lett. B **766**, 107 (2017)
[18] G. C. Li, Q. B. Chen, S. Q. Zhang *et al.*, Phys. Rev. C **100**, 044318 (2019)
[19] K. Y. Ma, J. B. Lu, J. Li *et al.*, J. Phys. G: Nucl. Part. Phys. **47**, 085106 (2020)
[20] Y. Y. Cheng, S. Q. Zhang, X. Q. Li *et al.*, Phys. Rev. C **89**, 054309 (2014)
[21] A. R. Vernon, R. F. Garcia Ruiz, T. Miyagi *et al.*, Nature **607**, 260 (2022)
[22] J. Karthein, C. M. Ricketts, R. F. Garcia Ruiz *et al.*, Nat. Phys. **20**, 1719 (2024)
[23] S. Y. Wang, D. P. Sun, B. T. Duan *et al.*, Phys. Rev. C **81**, 017301 (2010)
[24] S. Y. Wang, B. Qi, D. P. Sun *et al.*, Phys. Rev. C **82**, 057303 (2010)
[25] S. Y. Wang, D. P. Sun, B. Qi *et al.*, Phys. Rev. C **86**, 064302 (2012)
[26] L. Liu, S. Y. Wang, Z. Q. Chen *et al.*, Phys. Rev. C **90**, 014313 (2014)
[27] P. Vaska, D. B. Fossan, D. R. LaFosse *et al.*, Phys. Rev. C **57**, 1634 (1998)
[28] S. Naguleswaran, R. S. Chakrawarthy, U. Garg *et al.*, Phys. Rev. C **72**, 044304 (2005)
[29] Y. D. Fang, Y. H. Zhang, X. H. Zhou *et al.*, Phys. Rev. C **84**, 017301 (2011)
[30] W. Z. Xu, S. Y. Wang, X. G. Wu *et al.*, Phys. Lett. B **839**, 137789 (2023)
[31] R. M. Clark, L. W. Phair, M. Descovich *et al.*, Phys. Rev. C **72**, 054605 (2005)
[32] M. Piiparinen, A. Atac, J. Blomqvist *et al.*, Nucl. Phys. A **605**, 191 (1996)
[33] A. Gavron, Phys. Rev. C **21**, 230 (1980)
[34] O. B. Tarasov and D. Bazin, Nucl. Instrum. Methods Phys. Res. Sect. B **204**, 174 (2003)
[35] S. Y. Wang, B. T. Duan, X. X. Zhu *et al.*, Chin. Phys. C **33**, 838 (2009)
[36] D. P. Sun, H. F. Bai, W. Z. Xu *et al.*, Chin. Phys. C **46**, 092002 (2022)
[37] http://www.nndc.bnl.gov/ensdf/.
[38] M. D. Glascock, E. W. Schneider, W. B. Walters *et al.*, Phys. Rev. C **20**, 2370 (1979)
[39] C. W. Tang, A. Pakkanen, Z. C. Mester *et al.*, Z. Phys. A **272**, 301 (1975)
[40] A. Astier, M.-G. Porquet, Ts. Venkova *et al.*, Eur. Phys. J. A **30**, 541 (2006)
[41] Samit Bhowal, Chirashree Lahiri, Rajarshi Raut *et al.*, J. Phys. G: Nucl. Part. Phys. **38**, 035105 (2011)
[42] R. Lucas, M.-G. Porquet, Ts. Venkova *et al.*, Eur. Phys. J. A **15**, 315 (2002)
[43] S. Juutinen, R. Julin, P. Jones *et al.*, Phys. Lett. B **386**, 80 (1996)
[44] M. Kadi, N. Warr, P. E. Garrett *et al.*, Phys. Rev. C **68**, 031306(R) (2003)
[45] B. A. Brown, W. D. M. Rae, E. McDonald *et al.*, NUSHELLX@MSU, http://www.nscl.msu.edu/brown/resources/resources.html.
[46] P. W. Zhao, Z. P. Li, J. M. Yao *et al.*, Phys. Rev. C **82**, 054319 (2010)